Toward 3D Printing of Pure Metals by Laser-Induced Forward Transfer

Claas Willem Visser, Ralph Pohl,* Chao Sun, Gert-Willem Römer, Bert Huis in 't Veld, and Detlef Lohse*

Great progress in additive manufacturing technologies now allows the fabrication of complex 3D structures.[1] In particular, the printing concept has gained momentum for rapid prototyping, since it provides for fast, low-cost, and contact-free deposition at room conditions and poses minimal disturbances to the receiver substrate (on which the material is deposited). For instance, deposition of wax, polymers,[2] and even living cells[3] are now routinely achieved. However, printing of metals has been limited to low-melting point metals,[4–6] pastes,[7] and metal-containing inks,[8–10] which are generally not optimized in terms of material properties (e.g., mechanical strength, electrical conductivity, and corrosion rate) and material cost, or is still limited to the ≈1 mm resolution range.[11] Therefore, fabrication of metal microstructures including microantennas,[12] out-of-plane electrode production,[13] and filling of through-silicon vias (TSVs) for connecting stacked 2D electronic circuits[14] remain ongoing challenges.

Laser-induced forward transfer (LIFT) is a direct-write method allowing for drop-based deposition of a wide range of metals[15–19] including chromium,[20,21] tungsten,[20] gold,[22–24] nickel,[22] and aluminum.[25] Also pastes,[7,26] hydrogels,[27] and liquids[28–31] have been processed using LIFT, and, remarkably, similar ejection mechanisms seem applicable to these different material groups.[24,32] The concept is shown in **Figure 1**a. A pulsed laser is focused on the material to be transferred, called the "donor film," which is initially present on a transparent "carrier" substrate. The light is absorbed by the metal, resulting in a thermal stress wave or evaporation within a part of the film, which subsequently leads to the ejection of a liquid metal microdrop.[33] By placing a receiver substrate in the drop's line of flight, deposition is achieved. Up to now, pure-metal LIFT has enabled deposition of single drops,[32,34–36] lines,[14,37,38] and solid parts of the donor film.[20,39]

However, 3D metal printing using LIFT has been limited to low aspect ratio pillars,[40] perhaps since at least two challenging requirements have to be simultaneously fulfilled. First, good adhesion between stacked drops is required, but the deposited drops generally solidify in a spherical or torus shape.[14,32,34,35] This unavoidably results in porosity and limited drop-to-drop contact when the drops are stacked on top of each other. A second requirement is that the landing position of a single drop has to be limited to the previously deposited drop's impact area. This is nontrivial for the relatively large donor–receiver distances required for 3D printing,[41] but was achieved for a narrow range of fluences.

Here we manufacture pure-metal pillars by stacking micrometer-sized copper and gold drops. The morphological and physical features of the pillars are assessed in detail. We extend these results to the fabrication of extremely high aspect-ratio pillars, the filling of high-aspect ratio holes, and the deposition of an electrically conductive line. The relationships between the laser fluence, the drop impact velocity, and the drop shape after solidification are discussed, since these aspects are essential for controlled deposition. Finally, we present a concise outlook for fabrication of 3D metal structures using LIFT.

Figure 1a shows the setup used for laser-induced forward transfer. In short, a laser with a pulse duration of 6.7 ps and a wavelength of 515 nm is focused into a spot with a $1/e^2$ radius of 8.3 ± 0.5 µm, resulting in the melting and ejection of a 200 nm copper or gold film (see supplementary note 1A, Supporting Information, for details). As shown in two snapshots of an ejection event, the ejected material initially maintains its sheet-shape (Figure 1b), but strongly contracts by surface tension (Figure 1c), and eventually reaches a spherical shape. The drop ejection velocity ranges from 30 to 200 m s^{-1}, as we recently discussed.[33] The donor substrate is moved in the horizontal direction using a motorized translation stage. Repeated laser pulses then result in a series of ejection events at the same spatial position, which leads to the formation of a pillar if a receiver substrate is inserted below the donor.

The copper pillar shown in **Figure 2**a demonstrates the potential of LIFT for 3D metal micromanufacturing. The pillar has a height of around 80 µm and a diameter of 5.3 ± 0.7 µm. A halo of drops around the pillar is visible, due to drops passing the pillar tip or satellite droplet ejection (see Figure 1 and the supplementary movie of the Supporting Information). The pillar top is magnified in Figure 2b, showing the last-deposited drop which has spread out over the pillar top and subsequently solidified. Below this drop, the edges of several solidified drops are visible. To assess whether such round edges result in pores within the pillar, a pillar was cut lengthwise using a focused ion beam, and subsequently visualized using a scanning electron microscope (SEM) (for details, see supplementary note 1C, Supporting Information). As shown in Figure 2c,d, the

Dr. C. W. Visser, Prof. C. Sun, Prof. D. Lohse
Physics of Fluids Group, Faculty of Science and Technology
University of Twente
Drienerlolaan 5, 7500AE, Enschede, The Netherlands
E-mail: c.visser@utwente.nl

R. Pohl, Dr. G.-W. Römer, Prof. B. Huis in 't Veld
Chair of Applied Laser Technology, Faculty of Engineering Technology
University of Twente
Drienerlolaan 5, 7500AE, Enschede, The Netherlands
E-mail: r.pohl@utwente.nl

DOI: 10.1002/adma.201501058

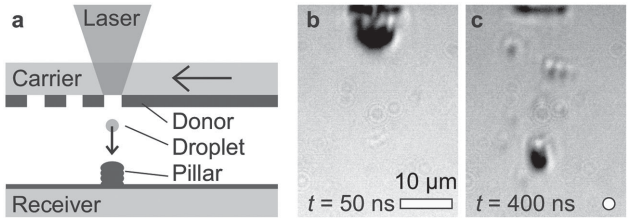

Figure 1. The LIFT concept. a) The LIFT setup. A laser pulse is focused onto a 200 nm thick copper donor layer, resulting in the ejection of a liquid copper drop (shown as a dot). By moving the glass carrier horizontally (shown by the arrow), repetitive ejections are induced at the same location. The impacting drops solidify, resulting in the formation of a pillar on the receiver substrate. The receiver is coated with a copper film, to improve the adhesion of the drop. Each ejection leaves behind a hole in the donor film: the "crater." b,c) A single LIFT ejection for fluence $F = (4600 \pm 200)$ J m^{-2}, 50 ns, and 400 ns after the laser pulse. The black area in the very top of these images shows the crater. In (b), the strongly deformed donor film is just detaching from the remaining substrate. In (c), the flying drop is shown, which is trailed by several smaller satellite drops. The drop appears to be much smaller than in (b), as surface tension contracts the (initially hollow) drop into a sphere with a final size as indicated by the white dot. Eventually, the drop will reach a spherical shape and land on the receiver substrate (not shown).

original drops are hardly visible and only a few small pores are observed. Using a through-lens detector, the grains within the pillar become just visible. Grains sizes between 50 and 200 nm are typically observed and seem to constitute most of the pillar volume. Furthermore, several long, horizontally aligned grain boundaries are identified, as illustrated by the dashed lines in Figure 2e. The ends of these boundaries (at the outer surface of the pillar) frequently coincide with voids corresponding to the edge of solidified drops. This footprint suggests that the impacting drops do not melt the pillar surface during impact, but instead crystallize onto the previously deposited drops. In principle, these horizontal interfaces could be weak or brittle. However, as the pillar can be bent significantly before plastic deformation occurs (see **Figure 3**b), the influence of these interfaces on the pillar characteristics seems to be limited.

Snapshots of the deposition process of a 270 µm high pillar are shown in Figure 3a (in the supplementary movie, Supporting Information, the drops are also visualized in-flight). In the final stage, the growth rate becomes constant as indicated by the inclined line in Figure 3a, and the pillar diameter is almost homogeneous. In the initial phase the pillar growth rate is suppressed, due to deviations in the ejection angle of the drop resulting in a spread of the impact location. Therefore, the bottom 30 µm of the pillar is slightly thicker. This thickening is easily prevented by reducing the donor–receiver distance by ≈50 µm, but could be beneficial if a strong pillar–receiver adhesion is required. The reproducibility of the pillars is illustrated in supplementary Figure 1, Supporting Information, showing five pillars on the same receiver substrate. These were deposited in a few minutes by moving the receiver and repeating a series of ejection events. Implementing an automated positioning stage for the receiver would readily allow for deposition of pillar–forests or complex microscale structures.

The homogeneity of the pillars and their thickness are assessed according to Figure 3b. By applying a controlled force and measuring the deflection of the pillar tip using an atomic force microscope, the effective thickness of the pillar is calculated to be 0.9 ± 0.15 µm (see supplementary note 1D, Supporting Information). The dashed line in Figure 3b indicates the calculated bending of a beam of homogeneous thickness, which collapses to the pillar shape. This confirms that the pillar is effectively homogeneous in thickness, despite its roughness and internal voids. The deformation of the pillar is elastic, illustrating that the pillar can be significantly deformed prior to plastic deformation.

The electrical resistance of the pillars is plotted in Figure 3c. The resistance was measured at different stages in the deposition process as illustrated in Figure 3a. The slope indicates the pillar resistance per unit length, which is normalized by the pillar area to provide the effective bulk resistance ρ_E (see supplementary note 1E, Supporting Information). For pillars processed in atmospheric conditions, $\rho_E = 35.3 \times 10^{-8}\ \Omega$ m, which exceeds the resistance of bulk copper (which is $\rho_E = 1.6 \times 10^{-8}\ \Omega$ m) by a factor of 22. As oxidation of the metal drops or the pillar tip during deposition was expected to cause this relatively high resistance, a next set of pillars was processed in an argon environment. As shown in Figure 3c, this approach reduces the bulk resistivity to $\rho_E = 18.7 \times 10^{-8}\ \Omega$ m, thus almost halves the resistance as compared to the air-processed pillars. The value of bulk copper is not obtained, presumably due to transfer of copper oxide from the donor film, (invisible) nanometer-scale inhomogeneities within the pillar (for example, gas bubbles that are entrained during droplet deposition,[42] or oxygen entering

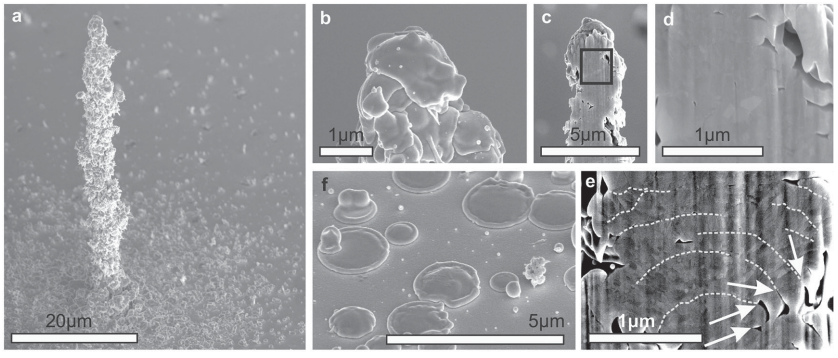

Figure 2. Copper pillar visualization. a) Overview image. Although the surface is rough, the thickness is relatively homogeneous. b) Pillar top, clearly showing the final drop which spread over the top prior to solidifying. The nanodrops visible on top of this drop are satellite drops caused during the ejection process. c) Cross section (obtained by cutting with a focused ion beam) of the pillar top; the region in the rectangle is magnified in (d) showing that the interior of the pillar is almost pore-free. e) Pillar cross section, showing different grain orientations in different color. Grain boundaries with a length spanning multiple grains are indicated as dashed lines. These lines typically end at pores in the edge of the pillar, which correspond to the original drop's edges. Therefore, these long grain boundaries likely correspond to the original drop's surfaces. f) Example view of solidified drops deposited next to a pillar. Images (a,c,d) are from the same pillar (the other images are from different pillars processed using the same ejection parameters).

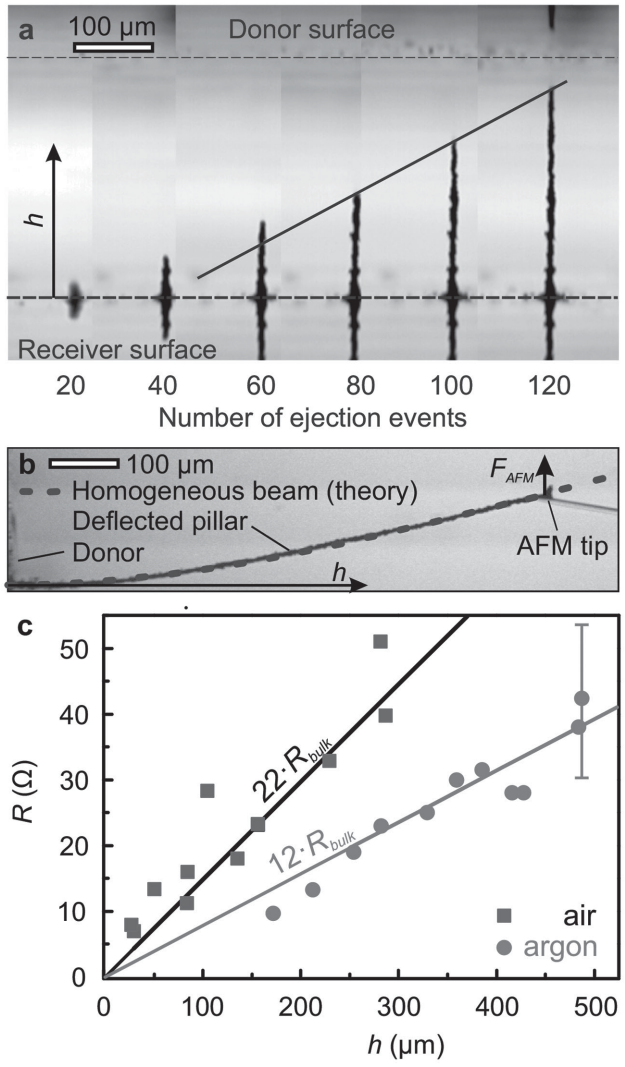

Figure 3. Pillar characterization. a) Snapshots of a pillar as a function of the number of ejections. The solid line indicates a constant pillar growth rate of 2.3 μm per ejection, which is observed if the pillar tip is sufficiently close to the donor surface and all drops land on the tip. b) Photograph of a pillar with a height h = 800 μm which is deflected by an AFM; the h-direction is indicated by the arrows in (a) and (b). The arrow at the AFM tip indicates the force (here F_{AFM} = 90 nN). The dashed line represents the modeled deflection of a homogeneous beam with a diameter of 2.2 μm. The agreement between this line and the pillar shape confirms the mechanical homogeneity of the pillar. c) Electrical resistance of pillars processed in air and argon as a function of the pillar height. The slope of the fitted lines indicates the resistance per unit length, which is 22 and 12 times higher than for bulk copper for the air- and argon-processed pillars, respectively. The error resulting from the ≈20% uncertainty in pillar thickness is indicated, and scales proportional to R.

through the top of the (partly open) argon container). Still, as both these values are several orders of magnitude below other metals used for printing of conductive wires (e.g., gallium–indium, for which $\rho_E = 3 \times 10^{-3}\ \Omega$ m,[43] the pillars printed here are suitable for out-of-plane electrode manufacturing.

To illustrate example applications, we extend the pillar deposition concept in the following. In **Figure 4**a, a 860 μm long pillar is deposited, by moving the receiver down during pillar deposition while maintaining a distance between the donor and the pillar tip in the range of 20–50 μm. Higher pillars can easily be created, until at some height the position of the tip is no longer stable. Here, small vibrations or light air flows result in swaying of the pillar. Therefore, a wider distribution in the drop impact location with respect to the tip is observed, resulting in a thicker tip. The longest (homogeneous) pillar we could deposit is 2.1 mm high and less than 5 μm in radius (see supplementary Figure 2, Supporting Information), providing an aspect ratio of at least 1:200. This pillar was deposited in gold. Next, the pillars can be deposited as out-of-plane interconnects between different layers of stacked electronics. A top view and cross section of such a TSV are shown in Figure 4f,g. The top view shows the virtually clean deposition process: Only a few drops landed next to the TSV, as indicated by the arrow. The TSV's cross section (Figure 4g) shows that the pillar extends to the 100 μm deep bottom. (As yet, we have only one visualization of a filled TSV, as their cutting without damaging the pillar proved highly challenging, e.g., the defect close to the top in Figure 4g might be caused by accidentally cutting the intact pillar.) Finally, high aspect ratios can also be achieved in the horizontal plane: by moving the receiver substrate while ejecting repeatedly a line is formed, shown in Figure 4h. The conductivity of these lines is 6 ± 2 times bulk copper. Controlling the receiver position also in the horizontal plane may enable truly 3D manufacturing, as discussed below.

The disk-shaped drops that constitute the pillars may be beneficial for 3D manufacturing, but these are not generally obtained. In particular, for fluences just above the ejection threshold a sphere is deposited, as shown in **Figure 5**a and reported previously.[14,16,32,34–36,44–46] For intermediate fluences, the drops solidify as a disk (Figure 5b,c), but toroids[34] and fragmentation[35,47] have also been observed (splashing, as shown in supplementary Figure 3, Supporting Information, is only scarcely observed; for a discussion see, e.g., ref. [42]). For even higher fluences, a transition occurs to spray ejection, in which many drops are ejected and deposited. Still, these drops individually solidify as a sphere, disk, or toroid as shown in Figure 5d and ref. [34]. Since the drop shape will affect the properties of any LIFT-printed structure, we will now assess this shape for various cases.

To assess why spherical deposition is usually observed for fluences just above the ejection threshold, we first calculate the ejection velocity at the ejection fluence threshold, and subsequently show that this velocity is insufficient to force the drop into a disk shape. Ejection occurs if the inertia of the ejected material exceeds the surface tension of the film, which is quantified by a threshold ejection Weber number,[33] $We_{ej} = phV_{ej}^2\sigma^{-1} \approx 1$, with donor film thickness h, density ρ, surface tension σ, and ejection velocity $V_{ej} \approx \sqrt{\sigma(\rho h)^{-1}}$. Next, to determine the drop shape during impact, we define an impact Weber number $We_{im} = \rho D_0 V_{im}^2 \sigma^{-1}$, describing the ratio between inertia and surface energy of the impacting drop. The diameter D_0 of the drop is generally of the same order as the film thickness (i.e., $D_0 < 10h$), and we assume that $V_{im} = V_{ej}$ (i.e., we neglect the effect of air drag), providing a maximum impact Weber number $We_{im} \approx 10$. For these low Weber numbers, drops hardly spread during impact[48] as shown in Figure 5e, and thus can only solidify in a spherical shape. Since fluences just above

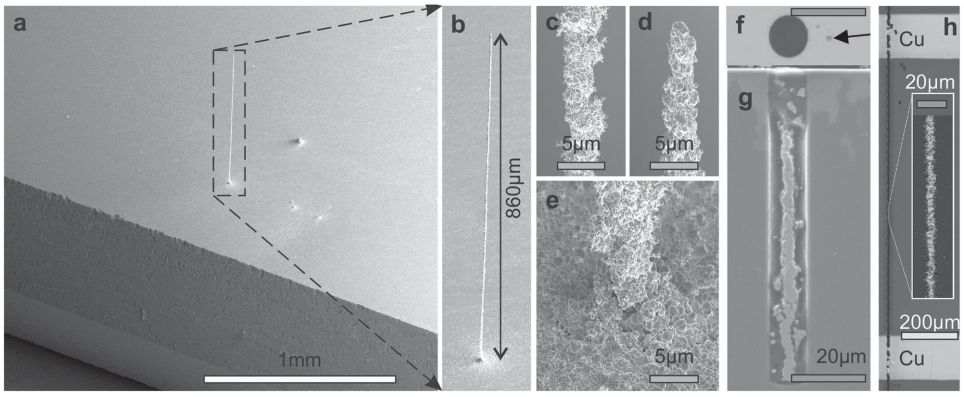

Figure 4. High-aspect ratio examples of copper LIFT. a) 860 µm long pillar close to the clearly visible edge of a microscope slide. b) Close-up of the pillar. Zooming in further shows that the pillar has a virtually homogeneous thickness: the center d) and top e) are around 4 µm thick whereas the bottom diameter (e) is around 6 µm, due to drops landing next to the pillar. f,g) A top view and a cross section of a filled TSV, respectively. The dark area next to the copper pillar (also visible from top) is a polymer for fixating the pillar, to avoid any harm due to grinding. The arrow in (f) indicates a droplet that landed next to the TSV. Image (g) shows that the pillar extends to the bottom of the hole. Finally, by moving the receiver substrate while depositing drops, copper lines that connect conductive pads were deposited on glass, as shown in (h). The inset shows a close-up of the line, in which the colors represent a height map.

the ejection threshold also correspond to the smallest droplets,[14,16,32,34–36,44–46] increasing the printing resolution (using smaller drops) and control of the drop shape are conflicting requirements.

For higher fluences, the impact velocity increases (i.e., $We \gtrsim 10$), resulting in inertial impact illustrated in Figure 5f–h. (An additional requirement for inertial impact is a high ratio of kinetic impact energy to viscous dissipation, which is represented by the Reynolds number $Re = \rho D_0 V_0 \mu^{-1}$, with viscosity μ. In LIFT, this condition is fulfilled since usually $Re \gtrsim 100$.) Initially, the drop spreads out into a disk, until a certain maximal spreading diameter D_{max} is reached as shown in Figure 5g. Meanwhile, the edge of the drop is contracting by surface tension, which results in the formation of an initially small "rim" shown in Figure 5g. This rim keeps growing until the drop reaches an essentially toroidal shape as shown in Figure 5h. Eventually, the drop contracts back into a spheroid that can even (partly) bounce away from the surface.[42] The sphere, disk, and toroids observed in LIFT (see Figure 5a–d) thus correspond to drop shapes for nonsolidifying impact.

The particular solidified drop shape will depend on the solidification time scale with respect to the spreading and retraction time scales of the drop. However, the solidification time scale cannot yet reliably be calculated (the spreading, retraction, and solidification time scales are discussed in supplementary note 2, Supporting Information). Therefore, we followed an empirical approach to optimize the drop shape. Initially, we tried to

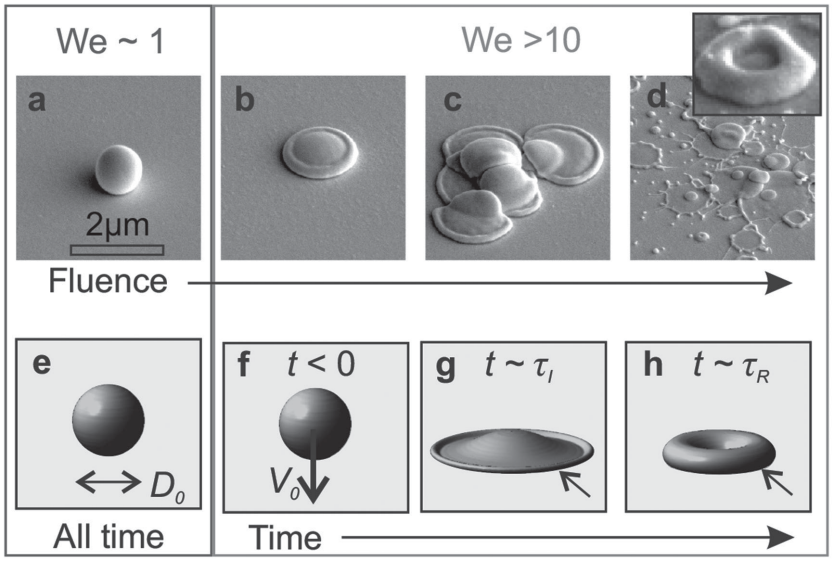

Figure 5. Drop shapes as a function of fluence, Weber number (*We*), and time. SEM images a–d) show solidified drops deposited on a copper-coated surface, for fluences of 3.8, 4.4, 6.3, and 8.2 kJ m^{-1}. Image (a) shows a droplet deposited just above the ejection fluence threshold. For these drops the Weber number is around 1, resulting in spherical solidification. For increasing fluence, droplets are deposited as a disk which is used to construct the pillars. Finally, a transition to spray ejection occurs resulting in the ejection of many drops, as shown in (d). In this regime, the solidification patterns include toroids, as illustrated in the inset (additional patterns are shown in supplementary Figure 3, Supporting Information). The scale bar of 2 µm holds for all images except the inset. e–h) Numerical simulations of impact dynamics onto nonwetting surfaces (surface not shown; for numerical details see supplementary note 1F, Supporting Information). Image (e) illustrates low Weber number impact (here, $We = 1$). In this low-velocity regime, the impact is dominated by surface tension and the drop maintains a spheroid shape. Images (f–h) illustrate the spreading dynamics of an impacting drop for the high Weber number case (here, $We = 150$). Image (f) shows the drop approaching the surface with velocity V_0. (g) The maximal spreading diameter is reached on the inertial time scale $\tau_1 \approx 2 V_0 D_0^{-1}$. (h) Subsequently, the drop retracts (snapshot shown for $t = 5 V_0 D_0^{-1}$) and the rim becomes dominant. The retraction occurs on the capillary time scale τ_R, as discussed in supplementary note 2, Supporting Information.

deposit the ejected drops onto a glass receiver, but then the drops bounce away. Since this bouncing effect was previously attributed to evaporation of volatile elements in the glass,[49] we coated the glass with a 100 nm thick copper film, resulting in disk-shaped solidification. This coarse approach is sufficient for pillar deposition, but we expect that further tuning of the film thickness and material allows to optimize the solidification time scale and thereby freeze the drop in any of the shapes discussed.

As seen, a trade-off exists between control of the drop shape, its impact location, and contamination. For fluences around the ejection threshold, clean deposition can be achieved but deposition will be spherical[14,16,32,34–36,44–46] due to the low Weber number. Moreover, we could not achieve drop stacking in this regime, since the impact location was insufficiently controlled for our donor–receiver distances of 10–100 µm. For fluences that significantly exceed the ejection threshold, the drop shape can be controlled as discussed in the previous paragraph, but here a single laser pulse generally results in the ejection of multiple drops. Remarkably, when significantly exceeding the ejection threshold fluence, these drops primarily land on top of each other as shown in Figure 5c. Our pillars have been deposited in this regime, since this behavior is consistent and the location of impact is robust with respect to the ejection location. At these fluences, small satellite drops are ejected and deposited around the main drop, resulting in contamination of the impact surface as observed in Figure 2a. A plausible cause of these undesired drops is uncontrolled break-up of the ejected cap from the metal film (see Figure 1b,c), which we aim to study in future work. Alternatively, nanosecond LIFT might allow for clean deposition, since highly aligned, satellite-free drops can be ejected at velocities allowing for disk-shaped solidification.[41,50]

Finally, the shape flexibility, resolution, and throughput of metal LIFT are concisely discussed. Spatially translating the receiver stage would allow for fabrication of rather complex 3D shapes, as already achieved by metal inkjet printing.[4] Implementing a rotating receiver stage may further expand shape flexibility, for example, to deposit horizontal pillar sections, arcs, or bridges. Printing has already been achieved for resolutions between 20 and 300 µm,[1,4,51] and is robust with respect to the drop size and material properties, since the drop impact dynamics is scale-invariant.[42] Metal LIFT extends this range down to length scales of 300–3 µm.[32,34,41] Since alternative technologies achieving micrometer resolution (such as stereolithography and laser chemical vapor deposition[52] require careful control of a surrounding fluid, this makes metal LIFT particularly interesting if processing under atmospheric conditions is required. In our system, the donor velocity of 2 mm s^{-1} and crater size of ≈10 µm limit the ejection frequency to 200 Hz, resulting in a volume ejection rate of ≈3 pl s^{-1}. However, the ejection rate can be substantially increased by scanning the laser position,[53] using a microlens array,[54] or using a thicker donor film.[41]

In summary, we control the deposition of copper and gold drops using LIFT, to construct pillars, lines, and fill through-silicon vias. The pillars, with diameters below 5 µm and lengths up to 2 mm, have a low porosity, are electrically conductive, and mechanically homogeneous. They consist of disk-shaped solidified drops, which is beneficial for 3D printing since the drop-to-drop contact area and adhesion are maximized. We show that disks are only obtained for laser energies that substantially exceed the ejection threshold, and explain why spherical deposition was observed in previous work. Remarkably, drop shape control and maximizing the printing resolution seem to be mutually exclusive requirements. By controlling both the position and angle of the receiver substrate, we expect that micromanufacturing of truly 3D structures would be achievable.

Supporting Information

Supporting Information is available from the Wiley Online Library or from the author.

Acknowledgements

C.W.V. and R.P. contributed equally to this work. Sander Wildeman is acknowledged for providing the drop impact simulations and Henk van Wolferen for operating the focused ion beam and SEM equipment. C.W.V., C.S., and D.L. acknowledge Fundamenteel Onderzoek der Materie (FOM) and the European Research Council (ERC) for funding. R.P., G.-W.R., and B.H.V. are grateful to the European Union Seventh Framework Programme for the funding under Grant Agreement No. 260079.

Received: March 3, 2015
Revised: April 14, 2015
Published online: June 5, 2015

[1] M. Vaezi, H. Seitz, S. Yang, *Int. J. Adv. Manuf. Technol.* **2013**, *67*, 1721.
[2] B.-J. de Gans, P. Duineveld, U. Schubert, *Adv. Mater.* **2004**, *16*, 203.
[3] S. Tasoglu, U. Demirci, *Trends Biotechnol.* **2013**, *31*, 110.
[4] K. Yamaguchi, K. Sakai, T. Hirayama, T. Yamanaka, *Precis. Eng.* **2000**, *24*, 2.
[5] W. Cao, Y. Miyamoto, *J. Mater. Proc. Technol.* **2006**, *173*, 209.
[6] C. Ladd, J.-H. So, J. Muth, M. D. Dickey, *Adv. Mater.* **2013**, *25*, 5081.
[7] J. Wang, R. C. Y. Auyeung, H. Kim, N. A. Charipar, A. Piqué, *Adv. Mater.* **2010**, *22*, 4462.
[8] J. Perelaer, P. J. Smith, D. Mager, D. Soltman, S. K. Volkman, V. Subramanian, J. G. Korvink, U. S. Schubert, *J. Mater. Chem.* **2010**, *20*, 8446.
[9] B. K. Park, D. Kim, S. Jeong, J. Moon, J. S. Kim, *Thin Solid Films* **2007**, *515*, 7706.
[10] S. H. Ko, J. Chung, N. Hotz, K. H. Nam, C. P. Grigoropoulos, *J. Micromech. Microeng.* **2010**, *20*, 125010.
[11] S.-y. Zhong, L.-h. Qi, J. Luo, H.-s. Zuo, X.-h. Hou, H.-j. Li, *J. Mater. Proc. Technol.* **2014**, *214*, 3089.
[12] J. J. Adams, E. B. Duoss, T. F. Malkowski, M. J. Motala, B. Y. Ahn, R. G. Nuzzo, J. T. Bernhard, J. A. Lewis, *Adv. Mater.* **2011**, *23*, 1335.
[13] Y.-C. Chiou, R.-T. Lee, T.-J. Chen, J.-M. Chiou, *Precis. Eng.* **2012**, *36*, 193.
[14] G. Oosterhuis, A. Prenen, A. J. Huis in't Veld, *ECS Trans.* **2012**, *41*, 81.
[15] V. Schultze, M. Wagner, *Appl. Phys. A* **1991**, *53*241.
[16] I. Zergioti, S. Mailis, N. Vainos, C. Fotakis, S. Chen, C. Grigoropoulos, *Appl. Surf. Sci.* **1998**, *127–129*, 601.

[17] P. Mogyorósi, T. Szörényi, K. Bali, Z. Tóth, I. Hevesi, *Appl. Surf. Sci.* **1989**, *36*, 157.
[18] H. Esrom, J.-Y. Zhang, U. Kogelschatz, A. J. Pedraza, *Appl. Surf. Sci.* **1995**, *86*, 202.
[19] Z. Tóth, T. Szörényi, A. Tóth, *Appl. Surf. Sci.* **1993**, *69*, 317.
[20] Z. Tóth, B. Hopp, T. Szörényi, Z. Bor, E. A. Shakhno, V. P. Veiko, *Proc. SPIE.* **1999**, *3822*, 18.
[21] I. Zergioti, D. Papazoglou, A. Karaiskou, C. Fotakis, E. Gamaly, A. Rode, *Appl. Surf. Sci.* **2003**, *208–209*, 177.
[22] T. Sano, H. Yamada, T. Nakayama, I. Miyamoto, *Appl. Surf. Sci.* **2002**, *186*, 221.
[23] Y. Nakata, T. Okada. *Appl. Phys. A* **1999**, *278*, 275.
[24] C. Unger, J. Koch, L. Overmeyer, B. N. Chichkov, *Opt. Express* **2012**, *20*, 24864.
[25] A. B. Bullock, P. R. Bolton, *J. Appl. Phys.* **1999**, *85*, 460.
[26] S. A. Mathews, R. C. Y. Auyeung, H. Kim, N. A. Charipar, A. Piqué, *J. Appl. Phys.* **2013**, *114*, 064910.
[27] F. Guillemot, A. Souquet, S. Catros, B. Guillotin, J. Lopez, M. Faucon, B. Pippenger, R. Bareille, M. Rémy, S. Bellance, P. Chabassier, J. C. Fricain, J. Amédée, *Acta Biomater.* **2010**, *6*, 2494.
[28] M. Colina, M. Duocastella, J. M. Fernández-Pradas, P. Serra, J. L. Morenza, *J. Appl. Phys.* **2006**, *99*, 084909.
[29] M. S. Brown, N. T. Kattamis, C. B. Arnold, *J. Appl. Phys.* **2010**, *107*, 083103.
[30] V. Dinca, A. Patrascioiu, J. Fernández-Pradas, J. Morenza, P. Serra, *Appl. Surf. Sci.* **2012**, *258*, 9379.
[31] C. Boutopoulos, I. Kalpyris, E. Serpetzoglou, I. Zergioti, *Microfluid. Nanofluid.* **2014**, *3*, 493.
[32] A. I. Kuznetsov, C. Unger, J. Koch, B. N. Chichkov, *Appl. Phys. A* **2012**, *106*, 479.
[33] R. Pohl, C. W. Visser, G.-W. Römer, D. Lohse, C. Sun, A. J. Huis in 't Veld, *Phys. Rev. Appl.* **2015**, *3*, 024001.
[34] D. P. Banks, C. Grivas, J. D. Mills, R. W. Eason, I. Zergioti, *Appl. Phys. Lett.* **2006**, *89*, 193107.
[35] L. Yang, C.-y. Wang, X.-c. Ni, Z.-j. Wang, W. Jia, L. Chai, *Appl. Phys. Lett.* **2006**, *89*, 161110.
[36] C. M. Othon, A. Laracuente, H. Ladouceur, B. R. Ringeisen, *Appl. Surf. Sci.* **2008**, *255*, 3407.
[37] K. Kordás, K. Bali, S. Leppävuori, A. Uusimaki, L. Nánai, *Appl. Surf. Sci.* **2000**, *154*, 399.
[38] C. Germain, L. Charron, L. Lilge, Y. Y. Tsui, *Appl. Surf. Sci.* **2007**, *253*, 8328.
[39] H. Yamada, T. Sano, T. Nakayama, I. Miyamoto, *Appl. Surf. Sci.* **2002**, *198*, 411.
[40] A. I. Kuznetsov, R. Kiyan, B. N. Chichkov, *Opt. Express* **2010**, *18*, 21198.
[41] M. P. Giesbers, M. B. Hoppenbrouwers, E. C. P. Smits, R. Mandamparambil, *Proc. SPIE* **2014**, *9135*, 91350Z.
[42] C. W. Visser, P. E. Frommhold, S. Wildeman, R. Mettin, D. Lohse, C. Sun, *Soft Matter* **2015**, *11*, 1708.
[43] D. Zrnic, D. Swatik, *J. Less-Common Met.* **1969**, *18*, 67.
[44] Y. Li, W. Ching-Yue, *Chin. Phys. B* **2009**, *18*, 10.
[45] A. Palla-Papavlu, V. Dinca, C. Luculescu, J. Shaw-Stewart, M. Nagel, T. Lippert, M. Dinescu, *J. Opt.* **2010**, *12*, 124014.
[46] D. A. Willis, V. Grosu, *Appl. Phys. Lett.* **2005**, *86*, 244103.
[47] A. Klini, P. A. Loukakos, D. Gray, A. Manousaki, C. Fotakis, *Opt. Express* **2008**, *16*, 11300.
[48] D. B. van Dam, C. Le Clerc, *Phys. Fluids* **2004**, *16*, 3403.
[49] A. McDonald, M. Lamontagne, C. Moreau, S. Chandra, *Thin Solid Films* **2006**, *514*, 212.
[50] A. Narazaki, T. Sato, R. Kurosaki, Y. Kawaguchi, H. Niino, *Appl. Phys. Express* **2008**, *1*, 057001.
[51] Y. P. Chao, L. H. Qi, Y. Xiao, J. Luo, J. M. Zhou, *J. Mater. Process. Technol.* **2012**, *212*, 484.
[52] O. Lehmann, M. Stuke, *Appl. Phys. A* **1991**, *53*, 343.
[53] E. Biver, L. Rapp, A.-P. Alloncle, P. Delaporte, *Appl. Surf. Sci.* **2014**, *302*, 153.
[54] G. Langer, D. Brodoceanu, D. Bauerle, *Appl. Phys. Lett.* **2006**, *89*, 261104.